When, what and how image transformation techniques should be used to reduce error in Particle Image Velocimetry data?

J.E. Higham

National Energy Technology Laboratories, Department of Energy, Morgantown, WV, USA.

W. Brevis

Department of Hydraulics and Environmental Engineering and Department of Mining, School of Engineering, Pontifical Catholic University of Chile, Santiago, Chile.

Abstract

Particle Image Velocimetry is commonly used to compute velocity fields in several areas including fluid mechanics, hydraulics and geophysics. However, acquired images often contain deformations caused either by camera lenses or placement. In this work the most popular digital transformation methods used to remove / reduce these deformations are benchmarked and suggestions tailoring specific transformations to different types of deformations are made. This article also shows the reduction of the error associated to the first and second order statistics, in the case of two-dimensional Particle Image Velocimetry, when the transformation techniques are applied to the computed velocity fields, and not the raw images, a common option in available commercial software.

Keywords: Particle Image Velocimetry, Image Registration, Image Processing, Digital Image Transformation

1. Introduction

In recent years an increased offer of inexpensive digital image sensors and the access to computational power has revolutionised science and technology. As a result, the use of image based techniques such as Particle Image Velocimetry (PIV) [1] in hydraulics [12], fluid mechanics [10] and geophysics [13] have become standard. The need for small image sensors, large field of views, and the occurrence of facilities-related optical distortions can lead to important deformations of the acquired images. Due to complex interactions of turbulent scales and the high accuracy required to quantify the dynamics of small-scale turbulence, any minor deformations in sensed images can lead to errors in the computed velocity

Email address: jonathan.higham@netl.doe.gov (J.E. Higham)

signals. Numerous previous works have have discussed and suggested strategies to correct the errors associated to two- (2D) and three-dimensional (3D) PIV measurements [25, 19, 11], however to the authors knowledge, there have been no previous contributions suggesting when, what and how image transformation techniques should be used to reduce camera deformations from PIV data. The correct selection of these transformation techniques is imperative, as different applications can cause different deformations, for which different transformation techniques are better suited. For example if a large image is being captured (e.g. [13]) large barrel deformations are created. Alternatively, when obtaining images for stereo/tomographic PIV or 3D Particle Tracking Velocimetry (PTV) ([25, 20]) different camera perspectives are required, leading to skew and perspective deformations. The correct choice and accuracy of these techniques is particularly important for certain applications of Tomographic PIV, where the raw images are used to self-calibrate the calculations and determine extremely small gradients [26]. Each image transformation technique works by the same premise, control points with known reference points, obtained from calibration targets, are used to create local transformation functions [6, 23, 14], global transformation functions,[7, 5], or locally weighted global transformations functions [8]. Whilst these methods offer reductions in error the range of the applicability of these techniques is yet to be determined, similarly there have been no investigations into the optimum number of control points for each method. Furthermore, in the case of 2D PIV, there is no general consensus as to whether the transformations should be applied to the raw sensed images or to computed the PIV velocity fields [27, 18, 4]; state-of-the-art commercial software normally apply the transforms to the raw images.

The present effort begins to tackle when, what and how images transformation techniques should be applied to reduce error. Whilst it is accepted that in methods such as stereo/tomographic-PIV or 3D-PTV applying these methods in 3D is also extremely important especially when there are changes in refractive index of a medium, for simplicity the main focus of the present study is on 2D, single camera based methods. To achieve this, a benchmark of the effectiveness of six variants of popular transformation techniques is undertaken to determine the optimal number calibration points. After this, the errors caused on the first and second order statistics, by transformation of either, the raw images or the estimated velocity components, is presented.

2. Geometrical transform techniques

In this section, the benchmarked transformation techniques are briefly outlined. Imaged control points are fitted to known co-ordinates via: a local transformation; a global transformation; or locally weighted global transformation. All of the transformations methods are applied individually to each image, i.e to an intensity field $\mathbf{I}(x, y)$ where $x = 1, 2, 3, \ldots, X$ and $y = 1, 2, 3, \ldots, Y$ are the spatial co-ordinates. The centroid position of the control points on the images are termed $\{\hat{x}_i, \hat{y}_i\}$ where $i = 1, 2, 3, \ldots C$ and C is the total number of control

points. These points are determined from the centroid of points on a calibration grid with known control point locations $\{u_i, v_i\}$.

2.1. Piecewise Linear transformation

The piecewise linear transformation is the simplest of the methods studied here. This method works by the triangulation of the two closest points to each i^{th} control point. The images are transformed using an affine transform via two local continuous functions $f_i(\hat{x}, \hat{y})$ and $g_i(\hat{x}, \hat{y})$:

$$\tilde{u} = f_i(\tilde{x}, \tilde{y}) = a_0\tilde{x} + a_1\tilde{y} + a_2 \tag{1}$$

$$\tilde{v} = g_i(\tilde{x}, \tilde{y}) = b_0\tilde{x} + b_1\tilde{y} + b_2 \tag{2}$$

where $\tilde{\cdot}$ represents the three triangulated points and $\{a_0, a_1, a_2, b_0, b_1 \ \& \ b_2\}$ are simply solved using a system of linear equations. As discussed by Goshtasby [9], if the local deformations are large, the gradients on two sides of a boundary greatly differ resulting in inaccurate transformations. Similarly, increasing the number of control points can increase the accuracy of the method, but reduce the computational efficiency. When applying this method in 3D, as shown by Calluaud and David [3], this method can also be used dewarp the out of plane co-ordinates and is often termed the pin-hole method.

2.2. Polynomial transformations

The polynomial transform is a global transformation method. This method uses all of the control points in the sensed image to created a single continuous n^{th} degree polynomial transform $\mathbf{f}(\hat{x}, \hat{y})$ from two bi-variate functions:

$$u = f(\hat{x}, \hat{y}) = \sum_{k=0}^{n}\sum_{l=0}^{l} P_{kl}\hat{x}^k\hat{y}^{k-l} \tag{3}$$

$$v = g(\hat{x}, \hat{y}) = \sum_{k=0}^{n}\sum_{l=0}^{l} Q_{kl}\hat{x}^k\hat{y}^{k-l} \tag{4}$$

where P and Q are coefficients. To solve for the $(d+1)^2$ coefficients at least $(d+1)^2$ independent pairs of points are required. Nack [17] and Van Wie and Stein [24] found that second or third order polynomials are sufficient for many applications, although Brown [2] and Zitova and Flusser [28] also note that too few points can create ill-fitting polynomials and too many can cause the polynomial to have large unexpected undulations.

2.3. Local weighted mean transformation

The local weighted mean transform devised by Maude [15] and McLain [16] uses localised second order polynomial transforms, $S_i(\hat{x}, \hat{y})$ (see previous) and

weight functions W_i, based on a neighbourhood of Z closest points around each i^{th} point, to create a global continuous smooth transform function:

$$W_i(\check{x},\check{y}) = \begin{cases} 1 - 3R^2 + 2R^3, & 0 \leq R \leq 1 \\ 0, & R > 1 \end{cases} \tag{5}$$

and

$$R = [(\check{x} - \hat{x}_i)^2 + (\check{y} - \hat{y}_i)^2)]^{\frac{1}{2}}/R_n \tag{6}$$

where $\check{\cdot}$ represents the points in the local neighbourhood and R_n is the closest point to the i^{th} point in the local neighbourhood. By applying this weight function to each of the local polynomials it is possible to create a continuous smooth function:

$$\mathbf{f}(\hat{x},\hat{y}) = \frac{\sum_{i=1}^{C} W(R_i) S_i(\check{x}_i,\check{y}_i)}{\sum_{i=1}^{C} W(R_i)} \tag{7}$$

Goshtasby [9] states this method is best suited to images with sharp geometric differences as the large number of small systems of equations better encode the image complexities, however, as a consequence the computational expense of the method is far greater.

3. Experimental setup

In the first set of experiments three different images are chosen to determine the optimal number of control points. The first image selected is the commonly used image processing 'Lena' image (Fig. 1a). The second is a synthetic PIV image generated using PIVLab [22] of a vortex ring, containing 10,000 synthetic PIV seed points with a mean pixel size of 3px (Fig. 1b). The third image is the streamwise component of the velocity field of the second set, calculated using PIVLab [22] using a double pass interrogation window ranging from 16px to 8px, with an overlap of 50% (Fig. 1c). Each image has spatial dimensions X=512 & Y=512. Due to the PIV calculations reducing the size of the image the original image (Fig 1b), the velocity field (Fig 1c) is resized using a nearest neighbour interpolation scheme to match the original data size. Four different synthetic deformations are applied to the images: (i) radial based barrel deformations (B); (ii) linear based perspective deformations (P); (iii) linear based skewing deformations (S) and (iv) a combination of all the above (BPS) (see Fig. 2). Each of these deformations are varied linearly with thirty scale factors and thirty different square grids of control points ranging from C={2-32}. B is linearly varied with a scale factor of 0-0.5 based on the central displacement as a function of the width of the image, P is linearly varied with a scale factor of 0-1.5 based on the width of the image, S is linear scaled with a scale factor of 0-1.5 based on the width of the image. BPS is implemented such that P=0.3, S=0.3 and B is varied from 0-0.5. In all of the cases a scale factor of 0 denotes no error. To remove / reduce the errors associated with these deformations six variants of the image transformations techniques are benchmarked: (i) Piecewise Linear (PWL); (ii) second order polynomial (POLY2);

(iii) third order polynomial (POLY3); (iv) fourth order polynomial (POLY4); (v) Local-weighted mean based on a neighbourhood Z= 12 (LWM12); and (vi) Local-weighted mean based on a neighbourhood Z= 24 (LWM24).

In the second set of experiments a sequence of PIV images are to used to investigate and quantify the effect on the first and second order statistics when the transformations are applied to either the raw images or the estimated velocity field. Here the first order statistics are defined as the two-dimensional, time averaged, streamwise flow and the second order statistics as the two-dimensional streamwise standard deviations. To quantify these effects eight combinations of B and P are applied to two hundred experimental images of a jet obtained from the PIV Challenge [21] with scale factors {0,0.25,0.5} and {0,0.5,1} respectively. All six variants of the transformations are applied either on the synthetically deformed raw images or on the computed velocity fields obtained from the raw synthetically deformed images. The PIV calculations are computed using a multi-pass interrogation window ranging from 32-16 px with an overlap of 50%. The total size of the raw images are 512×512 px.

To determine the error associated to the synthetically deformed images a framework for error quantification is required. Following [11] the relative errors ϵ_{DEF} & ϵ_{TRN} for the deformed image ($\mathbf{I}_{\mathrm{DEF}}$) and for the transformed image ($\mathbf{I}_{\mathrm{TRN}}$) are computed via:

$$\epsilon_{\mathrm{DEF}} = \sqrt{\frac{1}{XY}\sum_{x=1}^{X}\sum_{y=1}^{Y}\frac{(\mathbf{I}-\mathbf{I}_{\mathrm{DEF}})^2}{\mathbf{I}^2}}, \qquad \epsilon_{\mathrm{TRN}} = \sqrt{\frac{1}{XY}\sum_{x=1}^{X}\sum_{y=1}^{Y}\frac{(\mathbf{I}-\mathbf{I}_{\mathrm{TRN}})^2}{\mathbf{I}^2}}, \tag{8}$$

where each spatial location in $\mathbf{I}(x, y)$ represents either the intensity of the pixel in the first set of experiments or the first or second order statistics in the second set of experiments. In all cases a measure of removed error $E(\%)$ is defined as:

$$E(\%) = 1 - \frac{\epsilon_{\mathrm{TRN}}}{\epsilon_{\mathrm{DEF}}} \tag{9}$$

If the value of E = 0 no error has been removed, if E < 0 more error is produced, and E > 0 is the percentage error reduced.

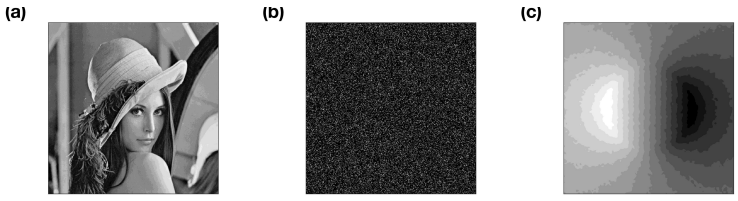

Figure 1: Benchmarking images: (a) 'Lena' image, (b) Synthetic image (c) computed streamwise velocity component from (b)

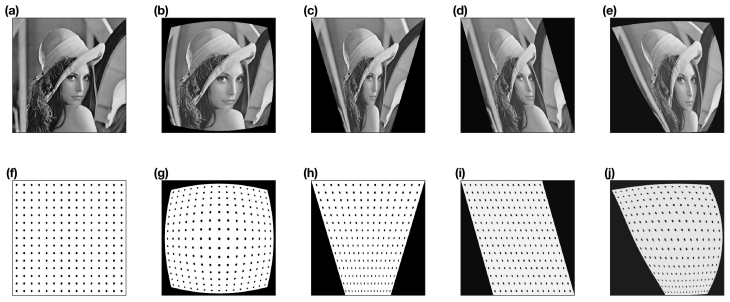

Figure 2: Examples of deformations applied to 'Lena' image. (a & f) Original image, (b & g) barrel transformed scale factor 1.1, (c & h) perspective deformation scale factor 0.8, (d & i) skew deformation scale 0.6, (e & j) combination of all previous.

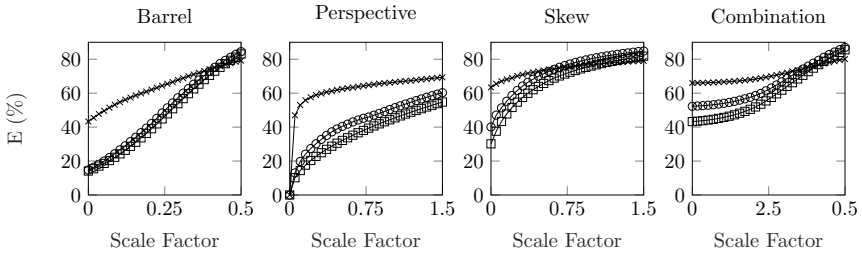

Figure 3: The percentage error ϵ_{DEF} induced in each image when the deformations are applied. Where ○ relates to the 'Lena' image, × relates to the raw PIV image and □ relates to the PIV velocity field.

4. Results

4.1. Single Images

Figure 3 shows the percentage error (ϵ_{TRA}) imposed in each image when synthetic deformations are applied by varying scale factors (here expressed as a percentage). The results show that the raw PIV data is most sensitive to deformations. The increase in error is likely explained by the intense gradients associated with the raw PIV images. As shown in Fig. 4 the effectiveness of the percentage error reduction is inversely proportional to the amount of error created by the synthetic deformations ϵ_{DEF} (as summarised in Fig. 3). The percentage reduction of error is far less in the raw PIV case, this might suggest that more accurate PIV results could be obtained when transforming the PIV vector fields and not the raw PIV images. When B is applied, quite clearly POLY2 is least effective in removing large distortions, although unlike the other methods the effectiveness of POLY2 is increased with a lesser number of control points. The higher order polynomials (POLY3 & POLY4) yield almost identical results, unlike POLY2 the reduction ability of the methods increase with more control points, although this converges at C∼15. In all of the polynomial cases

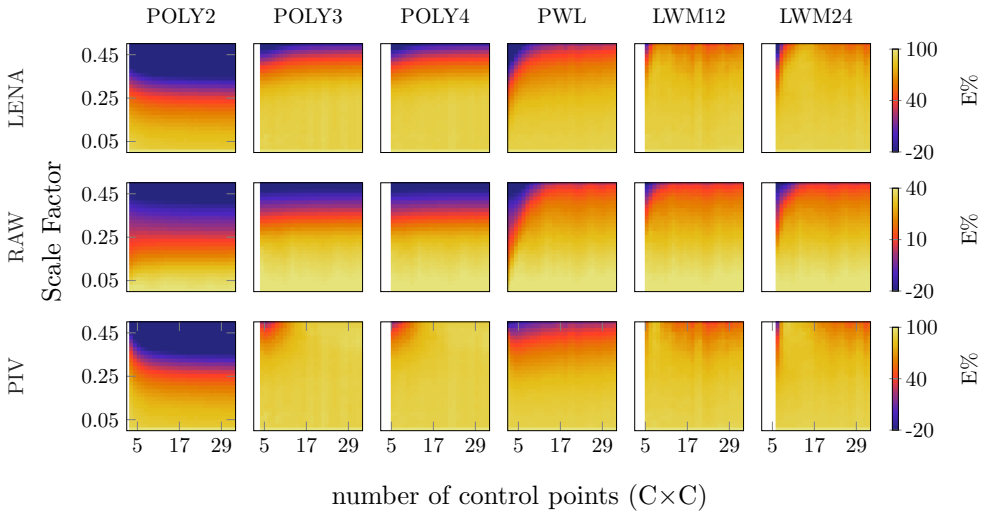

Figure 4: Results of different image transformation techniques applied to different scale factors of barrel deformation (B) and different number of control points (C × C). Each row relates to each of the three different images. The colour bar in each case represents the percentage of removed error (E%)

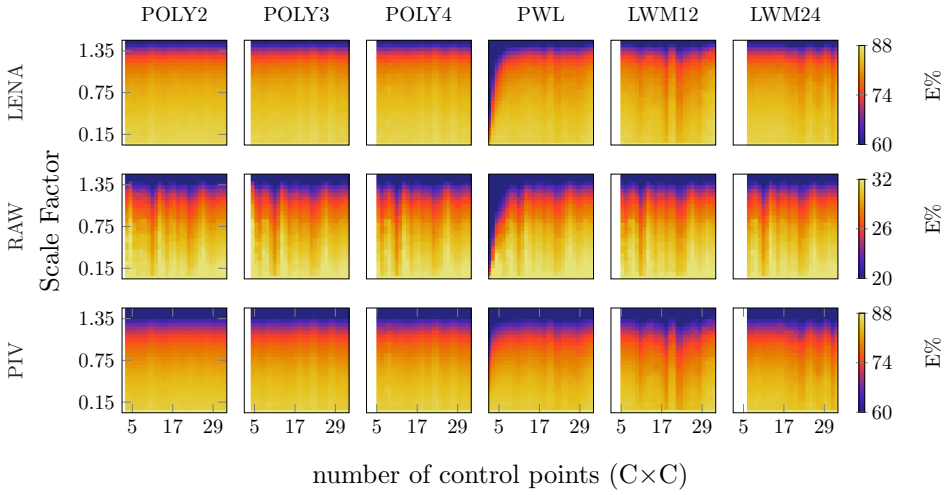

Figure 5: Results of different image transformation techniques applied to different scale factors of perspective deformation (P) and different number of control points (C × C). Each row relates to each of the three different images. The colour bar in each case represents the percentage of removed error (E%)

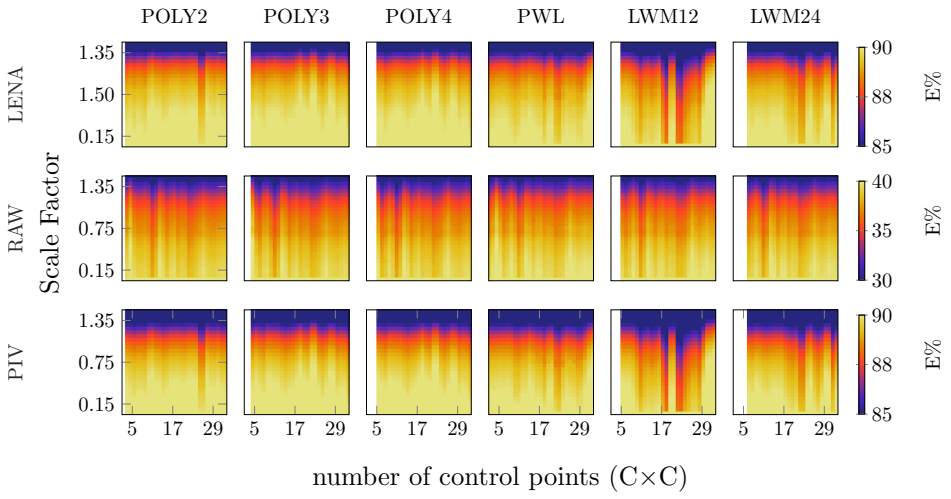

Figure 6: Results of different image transformation techniques applied to different scale factors of skew deformation (S) and different number of control points (C × C). Each row relates to each of the three different images. The colour map in each case represents the percentage of removed error (E%)

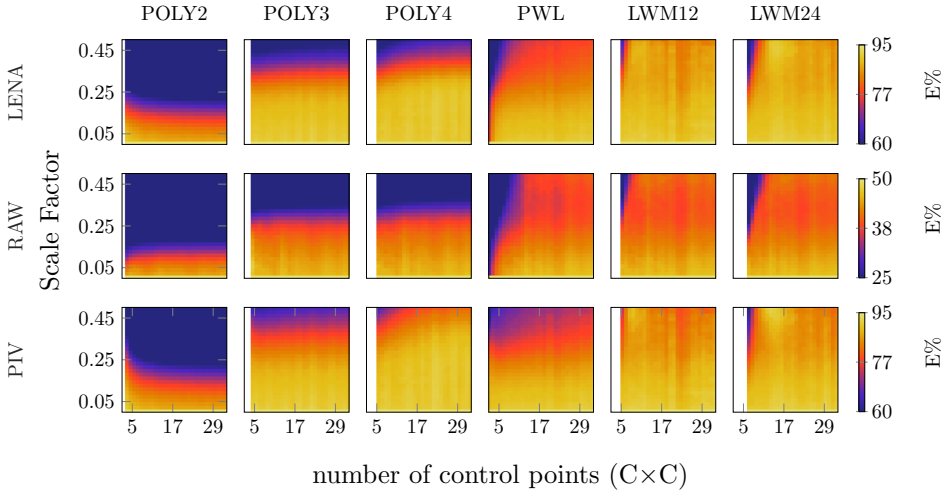

Figure 7: Results of different image transformation techniques applied to different scale factors of barrel deformation (B) combined with perspective deformation of scale factor (P=0.3) and skew deformation of scale factor (S=0.3) against different number of control points (C × C). Each row relates to each of the three different images. The colour map in each case represents the percentage of removed error (E%)

it is observed for extreme scale factors (POLY2 $\geq$ 0.25, POLY3 & POLY4 $\geq$ 0.30) the transformation methods actually create more error than they reduced. As expected for the PWL method increasing C increases the accuracy of the method, however, little differences are again noted with a C$\geq$15. Out of all of the methods LWM12 & LWM24 prove the most accurate with little difference between them, although with a C$\geq$15 their accuracy slightly reduces.

As shown in Fig. 5 P deformations are much more accurate even for scale factors which induce a similar ϵ_{DEF} as in B (see Fig. 3). All of the methods yield very similar results for each case, although C$\sim$10 is required for the PWL to achieve this accuracy. For the raw PIV images again all of the methods are least efficient which is likely to be associated to the high gradients in the images. In this case the LWM12 & LWM24 are least accurate when large scale factors of the deformations are applied. As shown in Fig. 6 the results are almost identical to those shown in Fig. 5, although for this case all the methods remove the most error even-though the average ϵ_{DEF} associated to this deformation is the greatest (see Fig. 3). The results for BPS, shown in Fig. 7, are very similar to those shown in Fig. 4, although no error is induced by any of the deformations. Similar to Fig. 4 LWM12 & LWM24 are most accurate and least sensitive to the increasing scale factor of the barrel deformations.

4.2. Image sequences

In Tables 1 & 2 the reduction of error obtained by applying all six variants of the transformation methods to eight combinations of scale factors of the synthetic B and P deformations are presented. As a consequence of the single image results highlighting an optimum value of C$\sim$15, this grid size is chosen. From the results it is clear that there are benefits transforming the PIV vector field and not the raw PIV images. This is particularly highlighted for the first order statistics. On average POLY3 achieves marginally favourable results. The benefits of applying the transformations methods to the PIV vector fields can be explained by Figs. 8 & 9 obtained using B = 0.25 & P = 0.75, as shown from in figures, particularly Fig. 8, when the transformations are applied to the raw PIV images visible radial distortions are present in the centre of the velocity fields. Similarly, as shown in Fig. 9 when the transformations are applied to the raw images outlier points are created, which are likely to induce a source or error.

5. Summary & Conclusions

In the present work the use of six variants of digital image transformation techniques for the removal of image deformations are benchmarked. By applying barrel, perspective and skew deformations with varying scale factors, it is found when images are radially deformed locally weighted global transformations using 15×15 control points are most effective in reducing error. When the images are linearly deformed either by a skew or perspective deformation, third and fourth order polynomial based transforms are more robust. This robust behaviour does

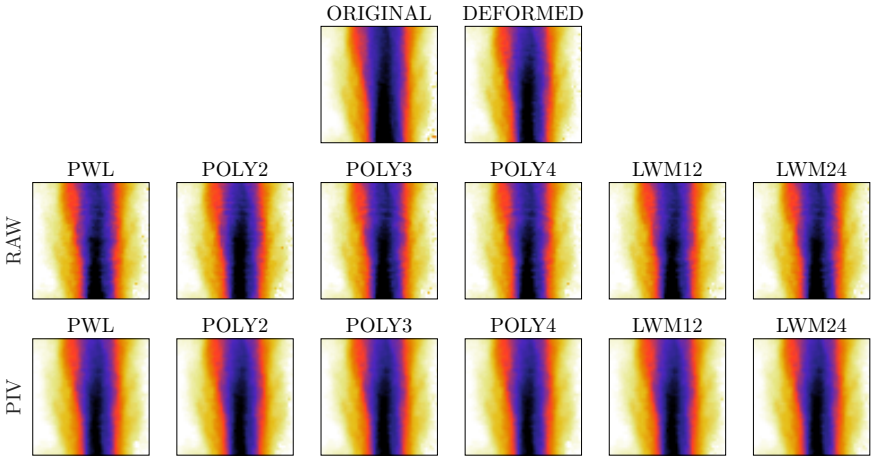

Figure 8: Time averaged streamwise velocity field. Top row shows the original and synthetically deformed images. Middle row shows results obtained from computing PIV vector fields from transformed raw images. Bottom row shows results obtained from transforming PIV vector fields.

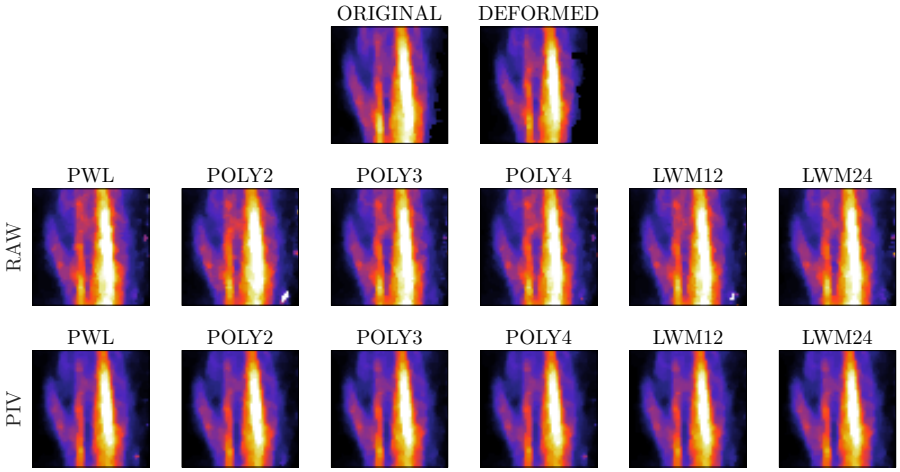

Figure 9: Temporal streamwise standard deviations. Top row shows the original and synthetically deformed images. Middle row shows results obtained from computing PIV vector fields from transformed raw images. Bottom row shows results obtained from transforming PIV vector fields.

Scale Factor			**RAW First Order** (E%)					
B	P	ϵ_{DEF}	PWL	POLY2	POLY3	POLY4	LWM12	LWM24
0.00	0.00	0.00	0.00	0.00	0.00	0.00	0.00	0.00
0.00	0.75	83.36	31.83	25.53	32.64	32.48	32.18	32.53
0.00	1.50	90.47	16.15	6.03	17.15	17.03	16.65	17.02
0.25	0.00	77.03	41.16	36.31	41.77	41.65	41.51	41.71
0.25	0.75	83.36	31.83	25.53	32.64	32.48	32.18	32.53
0.25	1.50	90.47	16.15	6.03	17.15	17.03	16.65	17.02
0.50	0.00	77.03	41.16	36.31	41.77	41.65	41.51	41.71
0.50	0.75	83.36	31.83	25.53	32.64	32.48	32.18	32.53
0.50	1.50	90.47	16.15	6.03	17.15	17.03	16.65	17.02

Scale Factor			**RAW Second Order** (E%)					
B	P	ϵ_{DEF}	PWL	POLY2	POLY3	POLY4	LWM12	LWM24
0.00	0.00	0.00	0.00	0.00	0.00	0.00	0.00	0.00
0.00	0.75	26.01	41.05	36.03	42.16	42.02	41.73	42.04
0.00	1.50	18.62	25.26	15.83	26.58	26.48	26.28	26.63
0.25	0.00	32.57	49.71	46.16	50.48	50.32	50.35	50.50
0.25	0.75	26.01	41.05	36.03	42.16	42.02	41.73	42.04
0.25	1.50	18.62	25.26	15.83	26.58	26.48	26.28	26.63
0.50	0.00	32.57	49.71	46.16	50.48	50.32	50.35	50.50
0.50	0.75	26.01	41.05	36.03	42.16	42.02	41.73	42.04
0.50	1.50	18.62	25.26	15.83	26.58	26.48	26.28	26.63

Table 1: Tables summarising error (E%) associated to the first and second order statistics obtained from performing PIV calculations on transformed images

not increase or decrease in accuracy for when more than 15×15 control points are used. Furthermore by applying synthetic combinations of deformations to a raw PIV image sequence it is found that the accuracy of first and second order statistics increased when the image transformations are applied to the computed vector fields rather than the raw images. This is likely explained by the PIV calculations smoothening out the sharp gradients associated to the image. In conclusion, if only radial deformations are present and or are large such, as in applications where a large image is sensed from a small sensor with a wide angle lens, a locally weighted method is suggested. If there are linear deformations and radial deformations are small, such as in the case of stereo and tomographic PIV, a high order polynomial method is suggested. In all cases it is suggested that a calibration plate with $\geq 15 \times 15$ control points is used. If a locally weighted method is used, no more than $\leq 20 \times 20$ controls points should be used. These results demonstrate the choice and application of image transformations technique can have significant impacts of the quality of and accuracy of the computed PIV vector fields. This accuracy is extremely important for tomographic and time-resolved PIV. Whilst the present work does

Scale Factor			**PIV First Order** (E%)					
B	P	ϵ_{DEF}	PWL	POLY2	POLY3	POLY4	LWM12	LWM24
0.00	0.00	0.00	0.00	0.00	0.00	0.00	0.00	0.00
0.00	0.75	83.36	46.37	42.70	46.44	46.39	46.40	46.40
0.00	1.50	90.47	34.78	28.41	34.83	34.82	34.86	34.84
0.25	0.00	77.03	53.27	50.80	53.38	53.30	53.29	53.29
0.25	0.75	83.36	46.37	42.70	46.44	46.39	46.40	46.40
0.25	1.50	90.47	34.78	28.41	34.83	34.82	34.86	34.84
0.50	0.00	77.03	53.27	50.80	53.38	53.30	53.29	53.29
0.50	0.75	83.36	46.37	42.70	46.44	46.39	46.40	46.40
0.50	1.50	90.47	34.78	28.41	34.83	34.82	34.86	34.84

Scale Factor			**PIV Second Order** (E%)					
B	P	ϵ_{DEF}	PWL	POLY2	POLY3	POLY4	LWM12	LWM24
0.00	0.00	0.00	0.00	0.00	0.00	0.00	0.00	0.00
0.00	0.75	26.01	49.28	47.85	49.30	49.25	49.28	49.26
0.00	1.50	18.62	36.65	32.89	36.65	36.60	36.70	36.64
0.25	0.00	32.57	55.92	55.28	55.99	55.92	55.90	55.91
0.25	0.75	26.01	49.28	47.85	49.30	49.25	49.28	49.26
0.25	1.50	18.62	36.65	32.89	36.65	36.60	36.70	36.64
0.50	0.00	32.57	55.92	55.28	55.99	55.92	55.90	55.91
0.50	0.75	26.01	49.28	47.85	49.30	49.25	49.28	49.26
0.50	1.50	18.62	36.65	32.89	36.65	36.60	36.70	36.64

Table 2: Tables summarising error (E%) associated to the first and second order statistics obtained from transforming PIV vector fields.

not fully answer, when, what and how images transformation techniques should be used to remove error in PIV data, it offers a guide for PIV users and provides evidence of the importance of a thorough selection of calibration methods.

6. Acknowledgements

Funding provided by Oakridge Institute for Science and Education. Also special thanks to Dr. Rogers for supporting the research.

[1] Adrian R J and Westerweel J 2011 *Particle image velocimetry* number 30 Cambridge University Press.

[2] Brown L G 1992 *ACM computing surveys (CSUR)* **24**(4), 325–376.

[3] Calluaud D and David L 2004 *Experiments in Fluids* **36**(1), 53–61.

[4] Giordano R and Astarita T 2009 *Experiments in fluids* **46**(4), 643.

[5] Glasbey C A and Mardia K V 1998 *Journal of applied statistics* **25**(2), 155–171.

[6] Goshtasby A 1986 *Pattern Recognition* **19**(6), 459–466.

[7] Goshtasby A 1987 *Pattern Recognition* **20**(5), 525–533.

[8] Goshtasby A 1988 *Image and Vision Computing* **6**(4), 255–261.

[9] Goshtasby A A 2005 *2-D and 3-D image registration: for medical, remote sensing, and industrial applications* John Wiley & Sons.

[10] Higham J and Brevis W 2018 *Experimental Thermal and Fluid Science* **90**, 212–219.

[11] Higham J, Brevis W and Keylock C 2016 *Measurement Science and Technology* **27**(12), 125303.

[12] Higham J, Brevis W, Keylock C and Safarzadeh A 2017 *Advances in Water Resources* .

[13] Hong J, Toloui M, Chamorro L P, Guala M, Howard K, Riley S, Tucker J and Sotiropoulos F 2014 *Nature communications* **5**.

[14] Keahey T A and Robertson E L 1996 *in* 'Information Visualization'96, Proceedings IEEE Symposium on' IEEE pp. 38–45.

[15] Maude A 1973 *The Computer Journal* **16**(1), 64–65.

[16] McLain D H 1976 *The Computer Journal* **19**(2), 178–181.

[17] Nack M 1977 *in* 'LARS Symposia' p. 174.

[18] Raffel M, Richard H, Ehrenfried K, Van der Wall B, Burley C, Beaumier P, McAlister K and Pengel K 2004 *Experiments in fluids* **36**(1), 146–156.

[19] Scarano F 2001 *Measurement science and technology* **13**(1), R1.

[20] Scarano F 2012 *Measurement Science and Technology* **24**(1), 012001.

[21] Stanislas M, Okamoto K, Kähler C J and Westerweel J 2005 *Experiments in Fluids* **39**(2), 170–191.

[22] Thielicke W and Stamhuis E 2014 *Journal of Open Research Software* **2**(1).

[23] Tsai C M and Yeh Z M 2008 *IEEE transactions on Consumer Electronics* **54**(2).

[24] Van Wie P and Stein M 1977 *IEEE Transactions on Geoscience Electronics* **15**(3), 130–137.

[25] Wieneke B 2005 *Experiments in fluids* **39**(2), 267–280.

[26] Wieneke B 2008 *Experiments in fluids* **45**(4), 549–556.

[27] Wieneke B 2015 *Measurement Science and Technology* **26**(7), 074002.

[28] Zitova B and Flusser J 2003 *Image and vision computing* **21**(11), 977–1000.